Enhanced spin Hall effect in S-implanted Pt

Utkarsh Shashank[#], Rohit Medwal[#], Taiga Shibata, Razia Nongjai, Joseph Vimal Vas, Martial Duchamp, Kandasami Asokan, Rajdeep Singh Rawat, Hironori Asada, Surbhi Gupta, and Yasuhiro Fukuma**
[#] Equal Contribution
* E-mail: sgupta@fukuma-lab.info, fukuma@cse.kyutech.ac.jp

Mr. U. Shashank, Mr. T. Shibata, Dr. S. Gupta, Prof. Y. Fukuma
Department of Physics and Information Technology, Faculty of Computer Science and System Engineering, Kyushu Institute of Technology, Iizuka 820-8502, Japan

Prof. Y. Fukuma
Research Center for Neuromorphic AI hardware, Kyushu Institute of Technology, Kitakyushu 808-0196, Japan

Dr. R. Medwal, Dr. J. V. Vas, and Prof. R. S. Rawat
Natural Science and Science Education, National Institute of Education, Nanyang Technological University, Singapore 637616, Singapore

Prof. H. Asada
Graduate School of Sciences and Technology for Innovation, Yamaguchi University, Ube 755-8611, Japan

Prof. M. Duchamp
Laboratory for In Situ & Operando electron Nanoscopy, School of Material Science and Engineering, Nanyang Technological University, Singapore

Dr. R. Nongjai and Dr. K. Asokan
Inter University Accelerator Centre, Aruna Asaf Ali Marg, New Delhi 110067, India

Keywords: Ion-implantation, spin Hall effect, spin-torque ferromagnetic resonance, spin-orbit-torque, spin Hall angle

Abstract

High efficiency of charge-spin interconversion in spin Hall materials is a prime necessity to apprehend intriguing functionalities of spin-orbit torque for magnetization switching, auto oscillations, and domain wall motion in energy-efficient and high-speed spintronic devices. To this end, innovations in fabricating advanced materials that possess not only large charge-spin conversion efficiency but viable electrical and spin Hall conductivity as well, are of importance. Here, we report a new spin Hall material designed by implanting low energy 12 keV Sulfur ions in heavy metal-Pt, named as Pt(S), which demonstrates 8-times higher conversion efficiency as compared to pristine Pt. The figure of merit, spin Hall angle (θ_{SH}), up to $\theta_{SH}^{Pt(S)}$ of 0.502 together with considerable conductivity $\sigma_{xx}^{Pt(S)}$ of 1.65×10^{6} $\Omega^{-1}m^{-1}$ is achieved. The spin Hall conductivity $\sigma_{SH}^{Pt(S)}$ increases with increasing $\sigma_{xx}^{Pt(S)}$, as $\sigma_{SH}^{Pt(S)} \propto \sigma_{xx}^{Pt(S)\,1.7}$, implying an intrinsic mechanism in a dirty metal conduction regime. The comparatively large $\sigma_{SH}^{Pt(S)}$ of 8.32×10^{5} $(\frac{\hbar}{2e})$ $\Omega^{-1}m^{-1}$ among the reported heavy-metals-based alloys can be useful for developing next generation spintronic devices using spin-orbit torque.

Controlled manipulation of magnetization using spin Hall effect (SHE), has recently brought substantial interest driven by the quest of fundamental physics involved to further meet technological advancements in the emerging field of magnetic memory and logics [1-4]. In heavy metal/ferromagnet (HM/FM) bilayer, upon charge current (J_c) injection, SHE induced spin-dependent accumulation at the interface leads to generation of transverse spin current (J_s) which exerts spin-orbit-torque (SOT) in FM layer enabling useful applications of magnetization switching, sustained oscillations, excitation of spin-waves and fast domain wall motion [4-6]. The spin current is given as $J_s = \frac{\hbar}{2e}\theta_{SH}(J_c \times \sigma)$, where θ_{SH} is spin Hall angle which quantifies the charge-spin interconversion efficiency and σ is the spin polarization. Continuous efforts have been made to find suitable HM exhibiting high θ_{SH} [7], but to reduce the energy consumption further, for the development of SOT-based spintronic devices, innovative ways of maximizing θ_{SH} with improved spin Hall conductivity are on high demand.

Practically, maximizing θ_{SH} requires a combined effort of first picking an amenable HM with a large intrinsic SHE and then increasing extrinsic scattering effects through interfaces, additives, and defects control are explored [7,8]. To date, Pt is more explored HM based spin Hall material (SHM) due to its large spin-orbit interaction and high conductivity [8-12] and has been previously engineered by oxidation [13], varying deposition conditions [14], and alloying with other metals [15-22]. For example, θ_{SH} is shown to be improved marginally from $0.044 \rightarrow 0.059$ by oxygen incorporation in Pt [13] whereas rigorously studied Pt-based alloys in combination to a variety of FM showed wide distribution in θ_{SH} values (in parentheses) like $Pt_{53}Au_{47}$/NiFe (0.33 ± 0.09) [15], $Pt_{75}Au_{25}$/Co (0.35) [16], $Pt_{75}Pd_{25}/Fe_{0.6}Co_{0.2}B_{0.2}$ (0.26 ± 0.02) [17], $Pt_{45}Pd_{55}$/NiFe (0.06) [18], $Pt_{90}Pd_{10}/Y_3Fe_5O_{12}$ (0.17) [19], $Pt_{85}Hf_{15}$/Co (0.16 ± 0.01) [20], $Pt_{92}Bi_8/Y_3Fe_5O_{12}$ (0.106 ± 0.005) [21] and $Pt_{28}Cu_{72}$/NiFe (0.07 ± 0.002) [22]. However, in this respect, ion-implantation or irradiation-

based engineering is not studied to tune the conversion efficiency of Pt despite being capable of molding spin-based properties such as local control of magnetization dynamics in NiFe/Pt [23], enhanced perpendicular anisotropy in Pt/Co/Pt [24], and reduced critical current for switching in Pt/Co/Ta [25].

Here, we report a new spin Hall material (SHM) fabricated by using non-metallic Sulfur-ion (S-ion) implantation in Pt, hereafter referred as Pt(S), at low energy of 12 keV with 5×10^{16} ions per cm^{-2} dosage. Combining spin-torque ferromagnetic resonance (ST-FMR) based spectral analysis and modulation of damping (MOD) measurements, we obtain exceptionally large 8-times (3 times) higher charge-to-spin conversion efficiency $\theta_{SH}^{Pt(S)}$ and 6-times (2-times) upshift in spin Hall conductivity $\sigma_{SH}^{Pt(S)}$ as compared to that of pristine Pt at 10 K (300 K). The inverse spin-to-charge conversion in Pt(S) is checked by mean of spin pumping-inverse spin Hall voltage (SP-ISHV) measurements and then the enhancement of $\theta_{SH}^{Pt(S)}$ is also confirmed. While the spin Hall conductivity of Pt, σ_{SH}^{Pt} is found to be independent of electrical conductivity σ_{xx}^{Pt}, $\sigma_{SH}^{Pt(S)}$ increases exponentially with increasing $\sigma_{xx}^{Pt(S)}$ as $\sigma_{SH}^{Pt(S)} \propto \sigma_{xx}^{Pt(S)\ 1.7}$. This result suggests that the dominant mechanism of SHE in Pt and Pt(S) is intrinsic in a metal conduction regime and in a dirty metal conduction regime, respectively [7, 26]. Therefore, Pt(S) is a compelling material and calls for new possibilities of implantation-engineering to artificially design an advanced family of SHMs that provide large charge-spin interconversion effect.

Firstly, multilayer stack of Pt (10 nm)/MgO (10 nm)/Al_2O_3 (10 nm) on Si/SiO_2 substrates was deposited at room temperature using ultra high vacuum magnetron sputtering. Secondly, the samples were implanted with 12 keV S-ion beam at fluence of 5×10^{16} ion/cm^2. The selected 12 keV energy of S-ions was pre-simulated using Transport of Ions in Matter (TRIM) code. Note that two capping layers of Al_2O_3 and MgO were purposefully deposited for two-fold benefits (1) least

perturbation of target-Pt layer while attaining throughout S-distribution and (2) precise ion-milling in follow-up step as MgO provides good end-point-detector signal whereas Al_2O_3 protects hygroscopic MgO from self-sputtering in S-implantation process. Cross-section transmission electron microscopy (TEM) image of pristine (**Figure 1**a) and implanted sample (**Figure 1**b) clearly show no significant change in interface quality and total thickness of target Pt layer. Further, high-resolution images in **Figure 1**c and **1**d dictates no visible loss in the polycrystallinity of Pt(S) in compare to pristine Pt deposited in fcc structure (see Fast Fourier Transform analysis in respective inset). Further energy filtered electron energy loss spectra (EELS) maps of host Pt ($O_{2,3}$ edge, 51.7 -63.7 eV) and implanted-S ($L_{2,3}$ edge, 165-182.1 eV) are shown in **Figure 1**e and **Figure 1**f respectively. Referring **Figure 1**f, we can see majority S-ions are stopped at capping MgO/Al_2O_3 layer and remaining are well dispersed throughout the target Pt layer, in agreement to TRIM simulations. The cross section of S and Pt were converted into atomic percentage based on the standard EELS spectra of the corresponding elements using the Gatan Microscopy Suite Software. The ratio of the S/Pt cross section with depth profile is given in the **Figure 1**g and the percentage of implanted S in Pt(S) layer is estimated to be ~10%. The X-ray photoemission spectroscopy (XPS) spectrum of Pt(S) plotted in **Figure 1**h shows the presence of native-Pt $4f_{7/2}$ and $4f_{5/2}$ peaks at 71.1 and 74.4 eV respectively, with smaller shoulder bands at 72.5 eV and 75.8 eV for Pt^{+2} that hints to sulfidation of Pt layer after implantation [27]. In detail, XPS results with depth profiling are provided in supplementary section S1. In final step, 10 nm thick $Ni_{80}Fe_{20}$ layer (hereafter referred as NiFe) is sputtered on both pristine Pt and Pt(S) layer after removing the capping (MgO/Al_2O_3) layers. The details are given in methods section.

ST-FMR measurements (see **Figure 2**a) were performed by applying microwave signal (f = 5 to 11 GHz) at 15 dBm in the presence of varying in-plane magnetic field (H_{ext} = -200 to 200

mT) at ϕ = 45°. The applied microwave signal generates oscillating H_{rf} and simultaneously converted oscillating spin current exerts respective Oersted field torque and SOT on local magnetization of the NiFe layer which collectively drive the magnetization dynamics, as depicted in **Figure 2**b. Upon satisfying a resonance condition, magnetization precession leads to a time-dependent change in resistance due to the anisotropic magnetoresistance (AMR) of NiFe. The AMR ratio is estimated to be ~ 0.69 % in present samples (refer supplementary section S2). The mixing of microwave current and oscillating resistance produces rectified DC voltage signal. Typical frequency dependent-rectified voltage spectra (V_{mix}) are plotted in **Figure 2**c, for both Pt/NiFe and Pt(S)/NiFe samples. The V_{mix} can be expressed as $V_{mix} = SF_{sym}(H_{ext}) + AF_{asym}(H_{ext})$ where $F_{sym}= \frac{\Delta H^2}{\Delta H^2+(H_{ext}-H_o)^2}$ defines an symmetric Lorentzian component and $F_{asym}= \frac{\Delta H\,(H_{ext}-H_o)}{\Delta H^2+(H_{ext}-H_o)^2}$ is an antisymmetric Lorentzian component, where S and A to be their weight factors, respectively, ΔH is the half width half maxima (HWHM) and the H_o is the resonance field [13,28]. As shown in **Figure 2**c, reversing the H_{ext} direction changes the sign of the V_{mix} signal as expected for spin-Hall voltage. A decrease in the amplitude of the V_{mix} signal for Pt(S)/NiFe as compared to Pt/NiFe is observed, as reported for Pt(O) [13] and Cu(O) [29]. The values of ΔH as a function of applied microwave frequency f are plotted in **Figure 2**d. The effective Gilbert damping parameter α is estimated, using $\Delta H = \Delta H_o + \frac{2\pi}{\gamma}\alpha f$, from the slope of the linear frequency dependence. Here, ΔH_o is the inhomogeneous line broadening. The estimated value of α, for Pt(S)/NiFe (0.0280 ± 0.0003) is larger than that for Pt/NiFe (0.0118 ± 0.0003), which indicates an enhanced spin injection into the Pt(S) layer. The variation of H_o as a function of f for Pt/NiFe and Pt(S)/NiFe is plotted in **Figure 2**e and effective magnetization ($4\pi M_{eff}$) is estimated using Kittel equation, $f = \gamma/2\pi\sqrt{H_o(H_o + 4\pi M_{eff})}$. The value of $4\pi M_{eff}$ is reduced from 965 mT

(for Pt/NiFe) to 778 mT (for Pt(S)/NiFe). This reduction in $4\pi M_{eff}$ can be understood in terms of an interface-perpendicular magnetic anisotropy [30].

The symmetric and anti-symmetric components of the V_{mix} signal obtained at f = 9 GHz for Pt/NiFe and Pt(S)/NiFe are plotted in **Figure 3**a and **3**b, respectively. The weight factor $S = \frac{\hbar J_S}{2e\mu_o M_S t}$ is proportional to the damping-like SOT, which is exerting an in-phase component with the magnetization precession, and the weight factor $A \approx \frac{J_C d}{2}\sqrt{1+\left(\frac{4\pi M_{eff}}{H_o}\right)}$ is attributed to the Oersted field torque exerting an out-of-phase component with it. Here e is electron charge, μ_o is permeability of the free space, t is thickness of the NiFe layer and d is thickness of the Pt or Pt(S) layer. A sharp increase in the relative amplitude of symmetric component for Pt(S) compared to Pt implies an increase of damping-like torque due to larger J_S. Furthermore, the ratio of injected J_S to applied J_C which effectively determines the conversion efficiency of SHM is given as $\theta_{SH}^{LS} = \frac{S}{A}\frac{e\mu_o M_S t d}{\hbar}\sqrt{1+\left(\frac{4\pi M_{eff}}{H_o}\right)}$ [13,28,29]. **Figure 3**c shows the estimated values of frequency invariant θ_{SH}^{LS} with average 3 times increase from 0.092 ± 0.008 (Pt) to 0.276 ± 0.011 (Pt(S)) after S implantation. The symmetric component in ST-FMR spectra might arise not only from the damping-like SOT but SP effect in which a precessing magnet (here NiFe) pumps a spin current back into SHM (here Pt or Pt(S)) where it is converted to a symmetric voltage output by spin-to-charge conversion. We found the SP contribution (V_{SP}) to be very less compared to symmetric weight factor S in Pt and Pt(S) respectively [refer supplementary section S3 for details]. Additionally, the antisymmetric component in the ST-FMR spectra is assumed here to be purely arising from Oersted field torque, which may not be valid in general. Therefore, we also performed modulation of damping (MOD) measurements to further confirm the conversion efficiency of Pt(S), defined as θ_{SH}^{LW}. The SOT being collinear to the damping either increase or decrease the linewidth depending upon the

injected spin polarization $\hat{\sigma}$ and the polarity of applied dc current I_{dc} [28]. The θ_{SH}^{LW} for Pt(S) is determined to be 0.354 ± 0.089 by probing the change in ΔH of the ST-FMR spectra under applied dc current range -0.4 mA ≤ I_{dc} ≤ 0.4 mA [refer supplementary section S4 for experimental details and analysis]. Note that, ST-FMR results from line shape and MOD measurements performed merely at $\phi = 45^{o}$ may not portrait the complete depiction of generated torques[31], and therefore the angular-dependent ST-FMR measurement was performed by varying in-plane H_{ext} direction from ϕ equal 0 to 360°. Angular dependence of both symmetric and antisymmetric component's weight factors is found to be in proportion to sin(2ϕ)cos(ϕ) for both Pt(S)/NiFe (refer **Figure 3**d) and Pt/NiFe [see supplementary section S5] which infers no symmetry-breaking for Oersted field torque and damping-like spin torque. To add, comprehensive investigation of spin pumping-inverse spin Hall voltage in out-of-plane configuration [32] also unveiled the enhancement of SHE in Pt(S). The anticipated three-time increased symmetric Lorentzian-voltage signal from Pt(S)/NiFe is obtained for studied microwave range (f = 5-11 GHz) in accordance with the ST-FMR results [refer supplementary section S6 for experimental details and analysis].

To gain a better understanding of underlying mechanism behind enhanced SHE in Pt(S) we carried out temperature (T) dependent ST-FMR measurements. **Figure** 3e and **3**f shows θ_{SH} as a function of T ranging from 300 to 10 K for Pt and Pt(S), respectively. The θ_{SH}^{Pt} shows a weak temperature dependence with slight decrease from 0.092 at 300 K to 0.064 at 10 K, is found to be consistent with earlier reports [33-35]. The inset of **Figure 3**e shows nearly invariant behavior of σ_{SH}^{Pt} with σ_{xx}^{Pt} that suggest an intrinsic origin of SHE in Pt in a metal conduction regime [7,14,26,34]. On the other hand, $\theta_{SH}^{Pt(S)}$ monotonically ramps up to 0.502 ± 0.016 with decreasing T and noticeably $\theta_{SH}^{Pt(S)}$ at 10 K becomes 8-times-higher than that for Pt. Also, continuous increase in $\sigma_{xx}^{Pt(S)}$ with

decreasing T conjointly results in 2.5-times enhanced $\sigma_{SH}^{Pt(S)}$ i.e. from 3.13 × 10^5 ($\frac{\hbar}{2e}$) $\Omega^{-1}m^{-1}$ at 300 K to 8.32 × 10^5 ($\frac{\hbar}{2e}$) $\Omega^{-1}m^{-1}$ at 10 K. The $\sigma_{SH}^{Pt(S)}$ versus $\sigma_{xx}^{Pt(S)}$plot fits well with the exponent factor (~1.7), as shown in the inset of **Figure 3**f. Such a scaling behavior with the exponent of 1.6-1.7 is reported for various materials with strong spin-orbit coupling in a dirty metal (or bad-metal) conduction regime [7, 26]. The implanted S ions in host Pt increase the charge scattering and then $\sigma_{SH}^{Pt(S)}$ decreases faster than $\sigma_{xx}^{Pt(S)}$ to obey a linear relationship in the strong disorder regime. Such a scattering does not suppress to obtain anomalous transverse velocity of the carrier and thus the observed $\sigma_{SH}^{Pt(S)} \propto (\sigma_{xx}^{Pt(S)})^{1.7}$ behavior implies an intrinsic origin of Pt(S), which may result in enhanced spin-orbit coupling. To further probe the explicit contribution, its band structure calculation would be needed.

Figure 4 summarizes θ_{SH} of Pt and Pt(S) in this study and other Pt derivative alloys as a function of σ_{xx} to provide bird-eye view. Pt shows highest SHE in pure metallic form, but the value of θ_{SH} is around 0.1 for its intrinsic mechanism [7,11,12,28,33]. By alloying or impurity doping in Pt, modified SHE and thus the enhancement of θ_{SH} is observed. In compare to Pt-Au alloys such as $Pt_{53}Au_{47}$ (0.33) [15] and $Pt_{75}Au_{25}$ (0.35) [16] the room temperature θ_{SH} for Pt(S) is slightly less, but at 10 K $\theta_{SH}^{Pt(S)}$ of 0.502 and $\sigma_{SH}^{Pt(S)}$ of 8.32 × 10^5 ($\frac{\hbar}{2e}$) $\Omega^{-1}m^{-1}$ is so far superior among Pt based SHMs including recent discoveries of $Pt_{92}Bi_8$ (0.106) [21], $Pt_{0.5}(MgO)_{0.5}$ (0.31) [36] and $PtTe_2$ (0.15) [37]. Moreover, the fabrication process for Pt(S) on Si/SiO_2 substrates such as sputtering and ion-implantation is compatible with CMOS technology, which is preferred for memory and logic applications, if compared to topological insulators like Bi_2Se_3 or $(Bi,Sb)_2Te_3$ on GaAs or/and sapphire substrates showing high conversion efficiency but also requiring molecular beam epitaxy systems [38, 39].

To summarize, we studied spin Hall effect in S-implanted Pt with 5×10^{16} ions per cm^{-2} dosage at low energy of 12 keV. The large $\theta_{SH}^{Pt(S)}$ of 0.502 along with high $\sigma_{SH}^{Pt(S)}$ of 8.32×10^5 $(\frac{\hbar}{2e})$ $\Omega^{-1}m^{-1}$ at reasonable conductivity $\sigma_{xx}^{Pt(S)}$ of 1.65×10^6 $\Omega^{-1}m^{-1}$ is explained as a consequence of effectively increased charge scattering as well as spin-orbit coupling after introducing S ions in Pt. Importantly, the enhancement of spin Hall effect is confirmed by multiple means i.e. line shape analysis and modulation of damping in spin-torque ferromagnetic measurements, and spin pumping-inverse spin Hall voltage measurements. Not only the large spin conductivity but also the good spin transparency at the Pt(S)/NiFe interface are a crucial factor to design new spintronic devices using spin-orbit-torque. We believe that these results encourage implantation-engineering as an effective tool to design custom-made spin Hall materials that can exert enhanced spin-orbit-torque by virtue of efficient charge-spin interconversion, indispensable in modern spintronics field.

Materials fabrication and characterization

Multilayer stack Pt (10 nm)/MgO (10 nm)/Al_2O_3(10 nm) was deposited on Si/SiO_2 substrates at room temperature using ultra high vacuum magnetron sputtering with base pressure ~ 5×10^{-7} Pa. Polycrystalline Pt layer is deposited at dc power of 50 W and Ar gas pressure of 1 Pa. Then sample is as transferred to an oxide deposition chamber for preparing MgO and Al_2O_3 capping layers under partial pressure of Ar and O_2 gas. Then deposited Pt/MgO/Al_2O_3 stacks was implanted with 12 keV-S ion-beam using 30 kV Tabletop Accelerator system. The optimized beam spot size of 15×15 mm^2 was used for the implantation in the samples with size of 10 mm × 10 mm. The JEOL Grand ARM equipped with a cold FEG gun and Gatan GIF Quantum 965 detector was used for TEM, STEM and EELS measurements. The XPS measurements were performed with Kratos AXIS Supra XPS that is equipped with an automated dual anode (Al/Ag Kα) X-ray monochromatic

source. The Pt/NiFe and Pt(S)/NiFe bilayer samples were patterned into micro-strips of dimensions 60×5 μm^2 using standard photolithography techniques for the ST-FMR measurements.

Acknowledgement

Authors thank Mr. Raj Kumar, IUAC for providing facilities for S ion implantation. Financial support from JSPS Grant-in-Aid (KAKENHI No. 18H01862, 18H05953, 19K21112) is gratefully acknowledged. This work is partially supported by Nippon Sheet Glass Foundation. R. M. would like to acknowledge research grant MOE-2017-T2-2-129. M.D. acknowledges the financial support from MOE-2019-T1-001-066. Transmission electron microscopy imaging and sample preparation were performed at the Facility for Analysis, Characterization, Testing and Simulation (FACTS) in Nanyang Technological University, Singapore. R. S. R would like to acknowledge research grant number MOE2017-T2-2-129, MOE2019-T2-1-058 and CRP21-2018-0093.

Received: ((will be filled in by the editorial staff))
Revised: ((will be filled in by the editorial staff))
Published online: ((will be filled in by the editorial staff))

References

[1] J. E. Hirsch, *Phys. Rev. Lett.* **1999**, *83*, 1834.

[2] S. O. Valenzuela, M. Tinkham, *Nature* **2006**, *442,* 176.

[3] Y. K. Kato, R. C. Myers, A. C. Gossard, D. D. Awschalom, *Science* **2004**, *306*, 1910.

[4] J. Ryu, S. Lee, K. J. Lee, B. G. Park, *Adv. Mater.* **2020**, 907148.

[5] B. Divinskiy, V. E. Demidov, S. Urazhdin, R. Freeman, A. B. Rinkevich, S. O. Demokritov, *Adv. Mater.* **2018**, 30, 1802837.

[6] A. Manchon, J. Železný, I. M. Miron, T. Jungwirth, J. Sinova, A. Thiaville, K. Garello, P. Gambardella, *Rev. Mod. Phys.* **2019**, *91*, 035004.

[7] A. Hoffmann, *IEEE Trans. Magn.* **2013**, *49*, 5172.

[8] L. Zhu, R. A. Buhrman, *Phys. Rev. Appl.* **2019**, *12*, 051002.

[9] E. Saitoh, M. Ueda, H. Miyajima, G. Tatara, *Appl. Phys. Lett.* **2006**, *88,* 182509.

[10] T. Kimura, Y. Otani, T. Sato, S. Takahashi, S. Maekawa, *Phys. Rev. Lett.* **2007**, *98,* 156601.

[11] M. H. Nguyen, D. C. Ralph, R. A. Buhrman, *Phys. Rev. Lett.* **2016**, *116*, 126601.

[12] W. Zhang, W. Han, X. Jiang, S. H. Yang, S. S. Parkin, *Nat. Phys.* **2015**, *11,* 496.

[13] H. An, T. Ohno, Y. Kanno, Y. Kageyama, Y. Monnai, H. Maki, J. Shi, K. Ando, *Sci. Adv.* **2018**, *4,* eaar2250.

[14] E. Sagasta, Y. Omori, M. Isasa, M. Gradhand, L. E. Hueso, Y. Niimi, Y. Otani, F. Casanova, *Phys. Rev. B* **2016**, *94*, 060412.

[15] M. Obstbaum, M. Decker, A. K. Greitner, M. Haertinger, T. N. G. Meier, M. Kronseder, K. Chadova, S. Wimmer, D. Ködderitzsch, H. Ebert, C. H. Back, *Phys. Rev. Lett.* **2016**, *117*, 167204.

[16] L. Zhu, D. C. Ralph, R. A. Buhrman, *Phys. Rev. Appl.* **2018**, *10*, 031001.

[17] L. Zhu, K. Sobotkiewich, X. Ma, X. Li, D. C. Ralph, R. A. Buhrman, *Adv. Funct. Mater.* **2019**, *29*, 1805822.

[18] X. Zhou, M. Tang, X. L. Fan, X. P. Qiu, S. M. Zhou, *Phys. Rev. B*. **2016**, *94*, 144427.

[19] L. Ma, H. A. Zhou, L. Wang, X. L. Fan, W. J. Fan, D. S. Xue, K. Xia, Z. Wang, R. Q. Wu, G. Y. Guo, L. Sun, X. Wang, X. M. Cheng, S. M. Zhou, *Adv. Elec. Mater.* **2016**, *2*, 1600112.

[20] M. H. Nguyen, M. Zhao, D. C. Ralph, R. A. Buhrman, *Appl. Phys. Lett.* **2016**, *108*, 242407.

[21] C. Hong, L. Jin, H. Zhang, M. Li, Y. Rao, B. Ma, J. Li, Z. Zhong, Q. Yang, *Adv. Electron. Mater.* **2018**, *4*, 1700632.

[22] R. Ramaswamy, Y. Wang, M. Elyasi, M. Motapothula, T. Venkatesan, X. Qiu, H. Yang, *Phys. Rev. Appl.* **2017**, *8*, 024034.

[23] A. Ganguly, S. Azzawi, S. Saha, J. A. King, R. M. Rowan-Robinson, A. T. Hindmarch, J. Sinha, D. Atkinson, A. Barman, *Sci. Rep.* **2015**, *5,* 17596.

[24] M. M. Jakubowski, M. O. Liedke, M. Butterling, E. Dynowska, I. Sveklo, E. Milińska, Z. Kurant, R. Böttger, J. von Borany, A. Maziewski, A. Wagner, A. Wawro, *Journal of Phys.: Conden. Mat.* **2019**, *31*, 185801.

[25] J. Yun, Y. Zuo, J. Mao, M. Chang, S. Zhang, J. Liu, L. Xi, *Appl. Phys. Lett.* **2019**, *115*, 032404.

[26] N. Nagaosa, J. Sinova, S. Onoda, A. H. MacDonald, N. P. Ong, *Rev. Mod. Phys.* **2010**, *82*, 1539.

[27] A. Romanchenko, M. Likhatski, Y. Mikhlin, *Minerals* **2018**, *8*, 578.

[28] L. Liu, T. Moriyama, D. C. Ralph, R. A. Buhrman, *Phys. Rev. Lett.* **2011,** *106*, 036601.

[29] Y. Kageyama, Y. Tazaki, H. An, T. Harumoto, T. Gao, J. Shi, K. Ando, *Sci. Adv.* **2019**, *5*, eaax4278.

[30] R. Medwal, S. Gupta, R. S. Rawat, A. Subramanian, Y. Fukuma, *Physica Status Solidi (RRL)–Rapid Research Lett.* **2019**, *13*, 1900267.

[31] J. Sklenar, W. Zhang, M. B. Jungfleisch, H. Saglam, S. Grudichak, W. Jiang, J. E. Pearson, J. B. Ketterson, A. Hoffmann, *Phys. Rev. B* **2017**, *95*, 224431.

[32] S. Gupta, R. Medwal, D. Kodama, K. Kondou, Y. Otani, Y. Fukuma. *Appl. Phys. Lett.* **2017**, *110*, 022404.

[33] Y. Wang, P. Deorani, X. Qiu, J. H. Kwon, H. Yang, *Appl. Phys. Lett.* **2014**, *105,* 152412.

[34] W. Zhang, M. B. Jungfleisch, W. Jiang, Y. Liu, J. E. Pearson, S. G. Te Velthuis, A. Hoffmann, F. Freimuth, Y. Mokrousov, *Phys. Rev. B* **2015**, *91*, 115316.

[35] M. Isasa, E. Villamor, L. E. Hueso, M. Gradhand, F. Casanova, *Phys. Rev. B* **2015**, *91*, 024402.

[36] L. Zhu, L. Zhu, M. Sui, D. C. Ralph, R. A. Buhrman, *Sci. Adv.* **2019**, 5, eaav8025.

[37] H. Xu, J. Wei, H. Zhou, J. Feng, T. Xu, H. Du, C. He, Y. Huang, J. Zhang, Y. Liu, H. C. Wu, C. Guo, X. Wang, Y. Guang, H. Wei, Y. Peng, W. Jiang, G. Yu, X. Han, *Adv. Mater.* **2020**, *32*, 2000513.

[38] A. R. Mellnik, J. S. Lee, A. Richardella, J. L. Grab, P. J. Mintun, M. H. Fischer, A. Vaezi, A. Manchon, E. –A. Kim, N. Samarth, D. C. Ralph, *Nature* **2014**, *511,* 449.

[39] K. Kondou, R. Yoshimi, A. Tsukazaki, Y. Fukuma, J. Matsuno, K. S. Takahashi, M. Kawasaki, Y. Tokura, Y. Otani, *Nat. Phys.* **2016**, *12,* 1027.

Figure captions:

Figure 1. Cross-sectional TEM image of (a) pristine $Si/SiO_2/Pt/MgO/Al_2O_3$ stack and (b) implanted $Si/SiO_2/Pt(S)/MgO/Al_2O_3$ stack unveil relatively no change in interface quality and thickness of target layer. High-resolution TEM shows polycrystalline nature of (c) Pt and (d) Pt(S)-layer. Inset shows respective Fast Fourier transform analysis. EELS elemental-mapping of (e) target-Pt and (f) implanted-S distribution in $Si/SiO_2/Pt(S)/MgO/Al_2O_3$ stack. (g) Histogram showing average atomic percentage of sulfur in platinum quantified by depth dependent S/Pt cross section. (h) Further fitted XPS spectrum for Pt(S) shows the presence of Pt^{2+} state as well.

Figure 2. Schematic illustration of a) ST-FMR detection with optical image of micro-device and b) SHE induced spin-torque effect. c) Frequency-dependent V_{mix} spectra for Pt/NiFe and Pt(S)/NiFe. d) ΔH versus f with linear fit (solid lines). e) f versus H_o with Kittel equation fit (solid lines).

Figure 3. Lorentzian fitting of ST-FMR spectra for a) Pt/NiFe and b) Pt(S)/NiFe into symmetric (blue) and antisymmetric (green) components. c) Frequency invariant θ_{SH}^{LS} for Pt/NiFe and Pt(S)/NiFe. d) Angular dependence of S and A components in ST-FMR spectra and corresponding $\sin2\phi\cos\phi$ fitting for Pt(S)/NiFe. Temperature dependent θ_{SH} variation for e) Pt/NiFe and f) Pt(S)/NiFe. First inset shows temperature invariant σ_{SH}^{Pt} behavior and second inset shows $\sigma_{SH}^{Pt(S)}$ versus $\sigma_{xx}^{Pt(S)}$ plot and corresponding non-linear fitting.

Figure 4. Bird-eye view showing reported θ_{SH} values for pure-Pt and its derivative alloys together with Pt(S) as a function of electrical conductivity σ_{xx}.

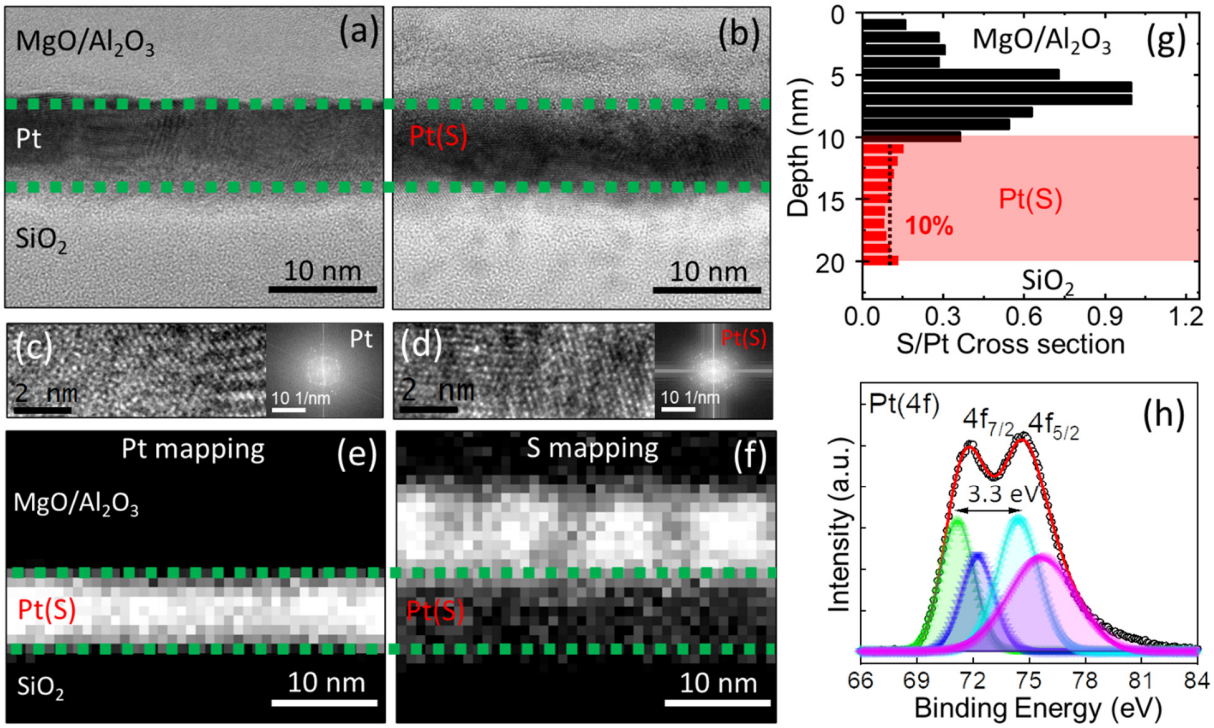

Fig. 1, U Shashank *et al.*

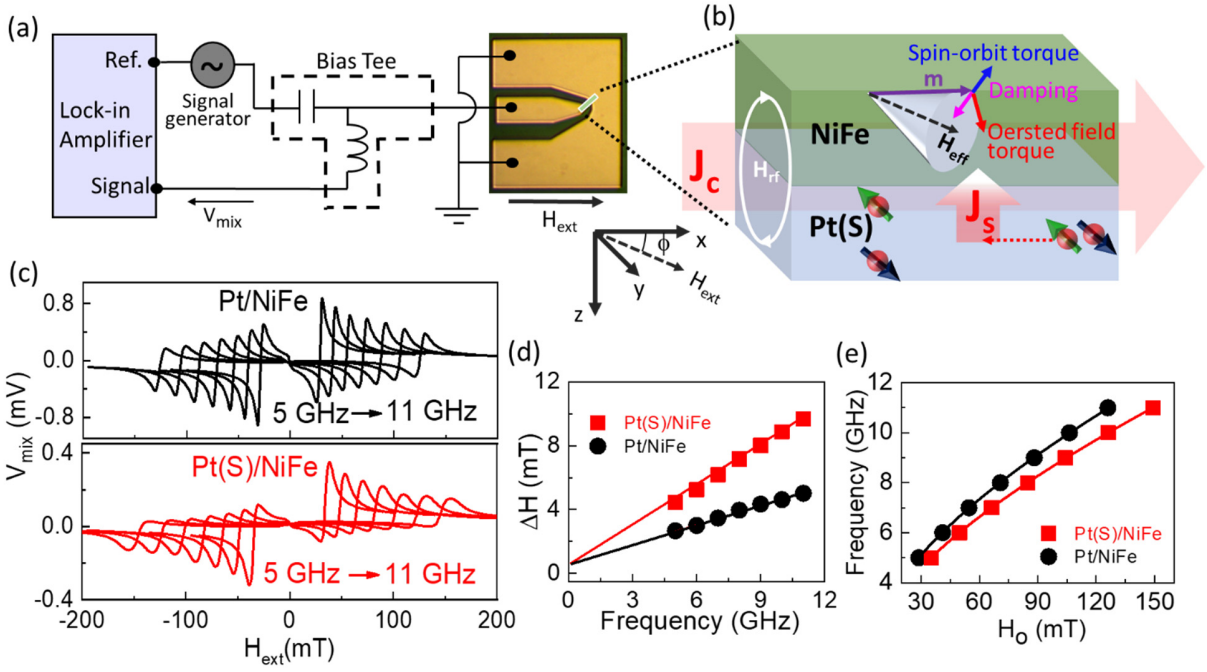

Fig. 2, U Shashank *et al.*

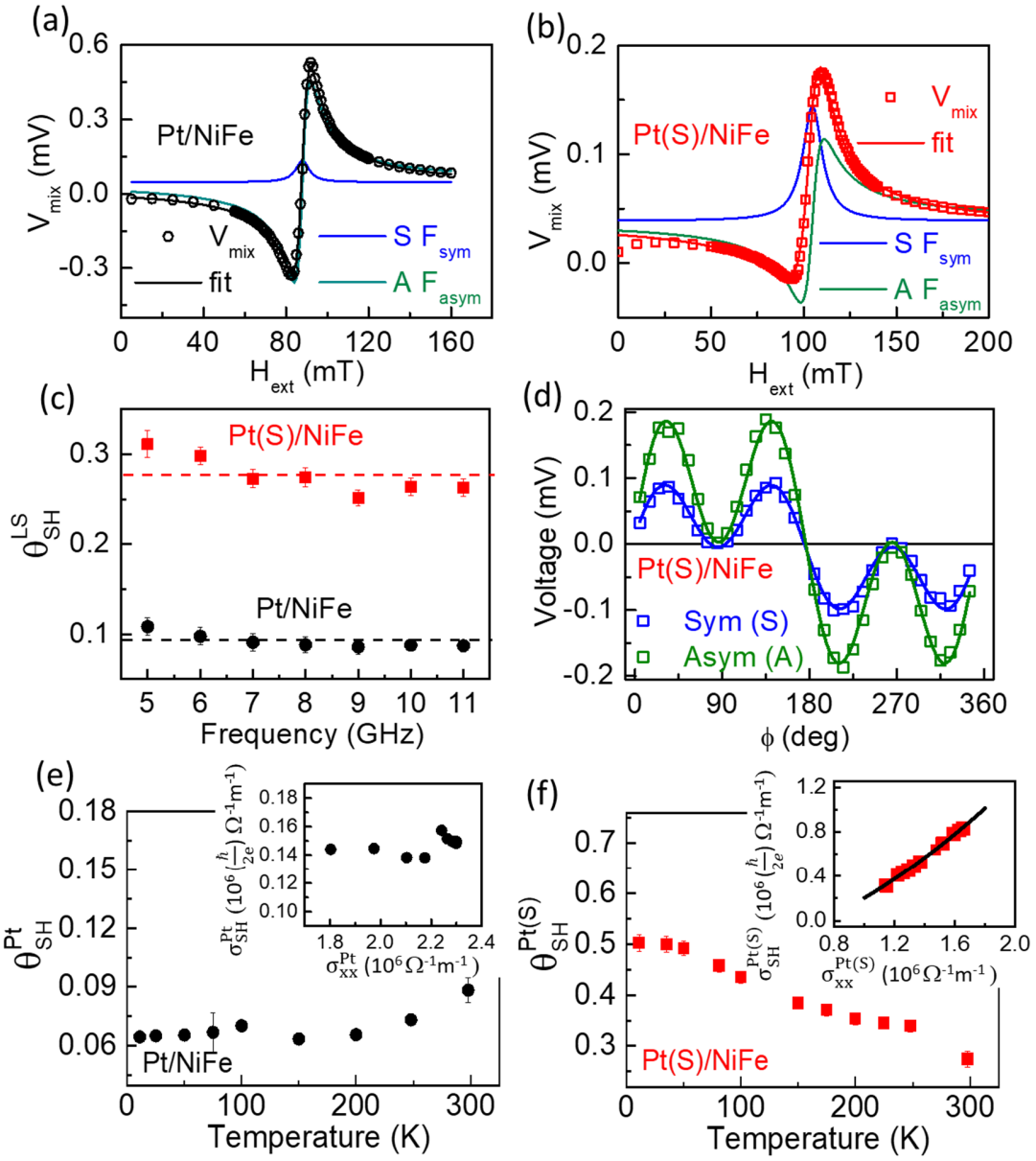

Fig. 3, U Shashank *et al.*

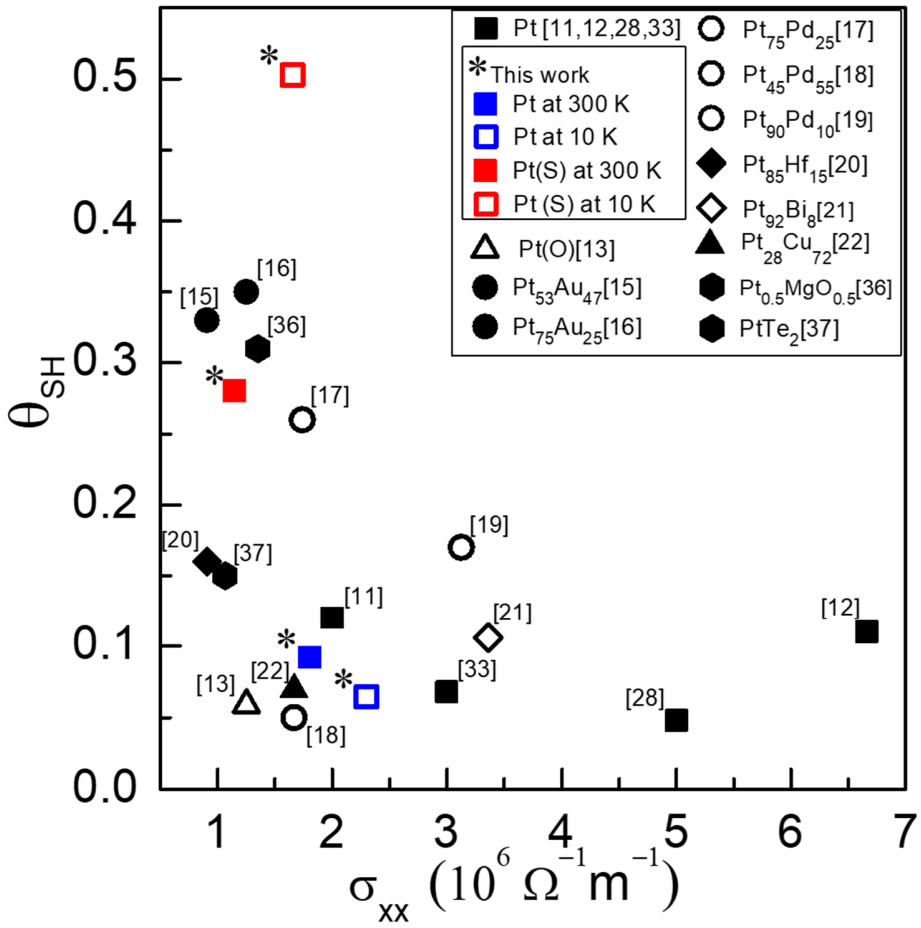

Fig.4, U Shashank *et al.*

Supplementary Information

Enhanced spin Hall effect in S-implanted Pt

Utkarsh Shashank[#], Rohit Medwal[#], Taiga Shibata, Razia Nongjai, Joseph Vimal Vas, Martial Duchamp, Kandasami Asokan, Rajdeep Singh Rawat, Hironori Asada, Surbhi Gupta, and Yasuhiro Fukuma**

Mr. U. Shashank, Mr. T. Shibata, Dr. S. Gupta, Prof. Y. Fukuma
Department of Physics and Information Technology, Faculty of Computer Science and System Engineering, Kyushu Institute of Technology, Iizuka 820-8502, Japan
E-mail: fukuma@cse.kyutech.ac.jp

Prof. Y. Fukuma
Research Center for Neuromorphic AI hardware, Kyushu Institute of Technology, Kitakyushu 808-0196, Japan

Dr. R. Medwal, Dr. J. V. Vas, Dr. S. Gupta and Prof. R. S. Rawat
Natural Science and Science Education, National Institute of Education, Nanyang Technological University, Singapore 637616, Singapore
E-mail: surbhi.gupta@nie.edu.sg

Prof. H. Asada
Graduate School of Sciences and Technology for Innovation, Yamaguchi University, Ube 755-8611, Japan

Prof. M. Duchamp
Laboratory for In Situ & Operando electron Nanoscopy, School of Material Science and Engineering, Nanyang Technological University, Singapore

Dr. R. Nongjai and Dr. K. Asokan
Inter University Accelerator Centre, Aruna Asaf Ali Marg, New Delhi 110067, India

#Equal Contribution

Keywords: Ion-implantation, spin Hall effect, spin-torque ferromagnetic resonance, spin-orbit-torque, spin Hall angle

Contents

Section S1: Etching time dependent core-level XPS study

Considering depth profiling using X-ray photoelectron spectroscopy (XPS), C(1s) spectra shows no shift in reference peak position with different etching time of 90-150 sec (see Fig S1(a)). However, up to 90 sec etching only Al(2p) peak is observed from capping layer (see Fig S1(b)) with S(2p) at 163.3 eV (see Fig S1(c)). This is followed by the evolution of two characteristic peaks corresponding to Pt (4f) core level after 120 sec etching and later two well-separated peaks of Pt($4f_{5/2}$) and Pt($4f_{7/2}$) at 71.1 and 74.4 eV respectively with energy difference of 3.3 eV matches well with spin-orbit splitting in Pt. While smaller shoulder bands at 72.5 eV and 75.8 eV for Pt^{+2} hints to sulphidation of Pt. In addition, the observed 0.8 eV shift in S(2p) binding energy also verifies the additional bond with host Pt.

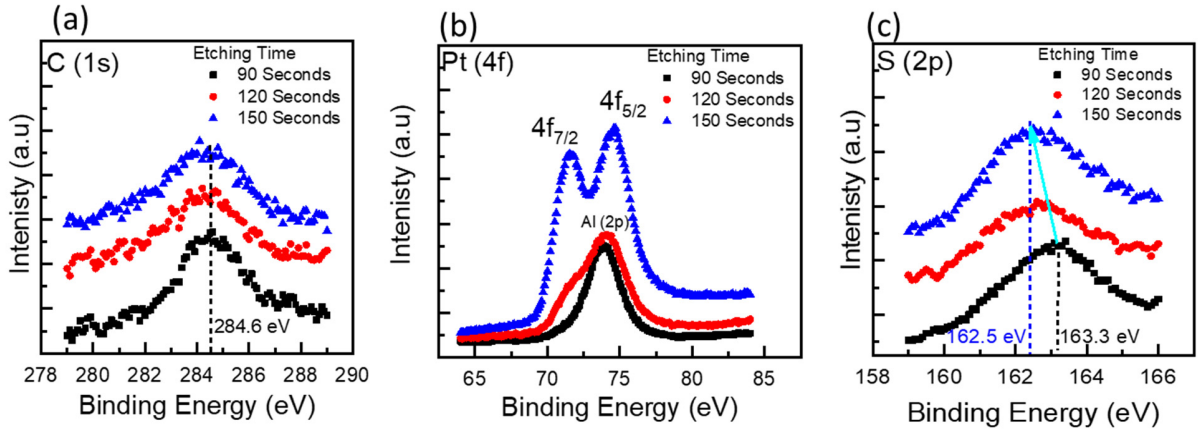

Figure S1: XPS emission spectra of **(a)** C(1s), **(b)** Pt(4f) and **(c)** S(2p) with different etching time.

Section S2: Magnetoresistance (MR) measurements

The amplitude of ST-FMR spectra is determined by the product of microwave signal and the change in resistance due to anisotropic magnetoresistance (AMR). So, to observe the change in resistance under applied dc magnetic field, we performed MR measurements. As shown in Fig. S2, the change in resistance $R[H_{ext}] - R[H_o]$ acquired for both parallel ($I \,||\, H_{ext}$) and perpendicular mode ($I \perp H_{ext}$) configuration, is plotted as a function of external magnetic field H_{ext} (from -125 mT to 125 mT). Here $R[H_{ext}]$ is the value of resistance at nonzero magnetic field and $R[H_o]$ is the value of resistance at zero magnetic field. The anisotropic magnetoresistance ratio (AMR) is calculated to be 0.69%.

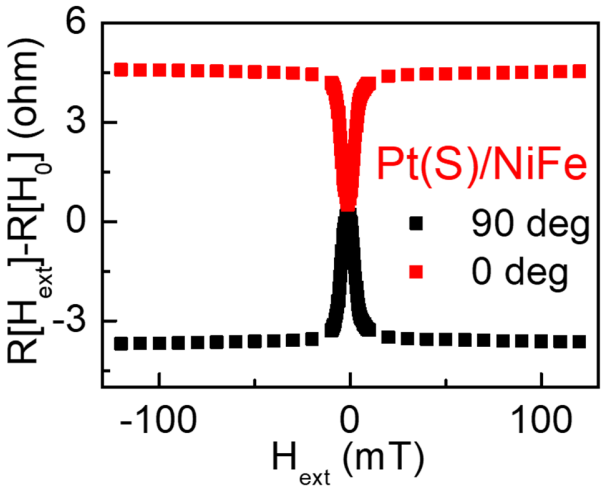

Figure S2: Magnetoresistance of Pt(S)/NiFe bilayer as a function of applied dc magnetic field.

Section S3: Separation of spin pumping contribution from ST-FMR signal

The influence of spin pumping contribution can be expressed as $V_{ISHE} = \frac{\theta_{SH} l \lambda_{sd}}{d\sigma_{SHM} + t\sigma_{NiFe}} \tanh\left(\frac{d}{2\lambda_{sd}}\right) \sin\phi$ where, θ_{SH} is the spin Hall angle of Pt and Pt(S), l is the length of the device, λ_{sd} is the spin diffusion length of SHE (Here either Pt or Pt(S)), d and σ_{SHM} are the thickness and conductivity of SHM layer, t and σ_{NiFe} are the thickness and conductivity of top ferromagnetic NiFe layer, e is the electronic charge, $\hbar$ is the reduced Planck constant, ϕ is the angle between external magnetic field and microwave current (45° in our case), J_S is the spin pumping current into the Pt(S) layer due to precessing NiFe given as $J_s = \frac{2e}{\hbar} \times \frac{\hbar\omega}{4\pi} g^{\uparrow\downarrow} \sin^2\theta_C \left[2\omega \frac{\left(\gamma M_S + \sqrt{(\gamma M_S)^2 + (2\omega)^2}\right)}{(\gamma M_S)^2 + (2\omega)^2}\right]$ where, $\omega = 2\pi f$ is the applied microwave frequency and $g^{\uparrow\downarrow}$ is the spin mixing conductance. While θ_C is the precession cone angle, estimated using $\theta_C = \frac{1}{dR/d\phi} \frac{2}{I_{rf}} \sqrt{S^2 + A^2}$ in which S and A are the voltage weight factors of symmetric and antisymmetric component, $dR/d\phi$ is obtained from angular magnetoresistance measurements, and I_{rf} is the microwave current in the device. The estimated spin pumping contribution V_{ISHE} is found to be 1.82 μV at 9 GHz which is much less compared to S = 95.72 μV for Pt(S)/NiFe while for control sample Pt/NiFe, V_{SP} is found to be 7.97 μV at 9 GHz which is also less compared to S = 101.88 μV. Therefore, SP contribution does not affect our estimation of θ_{SH}^{LS} using line-shape analysis.

Section S4: MOD ST-FMR measurements

To probe change in ΔH of ST-FMR spectra under additional DC current with microwave signal for Pt(S)/NiFe and Pt/NiFe, we performed DC biased ST-FMR measurements keeping ϕ at 45° as shown in the set-up image. **Figure** S3(a) shows selected spectra for Pt(S)/NiFe to highlight ΔH increase as I_{dc} is sequentially changed from -0.25 to 0.25 mA for negative H_{ext} direction (here, full range is not shown for brevity). Consequently, ΔH gets narrower for positive H_{ext} as seen in **Figure** S3(b). Noticeably, ΔH shows a linear variation with I_{dc} and slope gets reverse with slight swing when H_{ext} direction is 180° shifted to ϕ = 225°. The θ_{SH}^{LW} is determined to be 0.354 ± 0.089 using $\theta_{SH}^{LW} = \frac{\frac{2e}{\hbar}\left(H_o + \frac{M_{eff}}{2}\right)\mu_o M_S t\left|\frac{\Delta\alpha_{eff}}{\Delta J_C}\right|}{\sin\phi}$ [1] where $\Delta\alpha_{eff}$ implies to I_{dc} dependent change in effective damping. In case of Pt/NiFe sample, signal to noise ratio did not decrease significantly and we were able to apply higher DC current up to ± 0.8 mA. However, only small change in ΔH (around 0.15 mT) was observed (Refer **Figure** S3(c)) and correspondingly smaller θ_{SH} = 0.102 ± 0.040 is estimated. While we obtained a large change in ΔH (around 0.40 mT) for Pt(S)/NiFe under lower applied dc current range due to its large SHE.

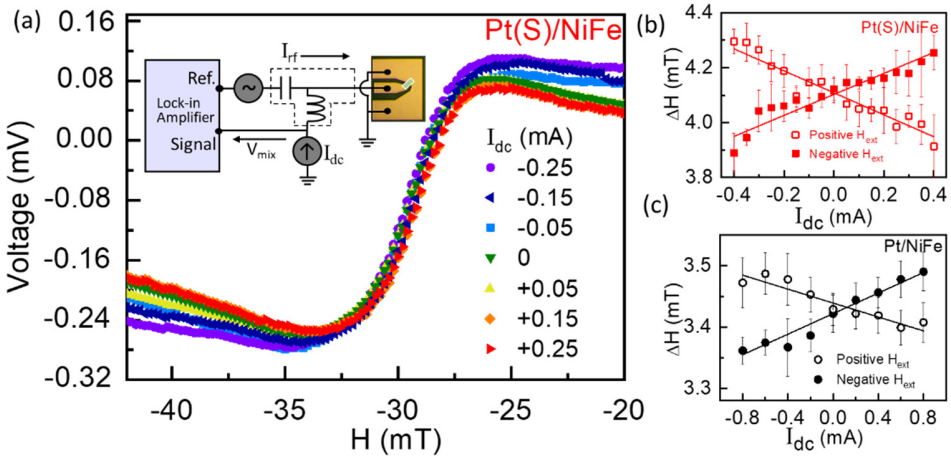

Figure S3: (a) Varying HWHM of ST-FMR spectra under I_{dc} range of ± 0.25 mA applied to Pt(S)/NiFe and obtained at f = 5 GHz. Inset shows MOD measurement set-up. Change in ΔH as a function of I_{dc} for b) Pt(S)/NiFe and c) Pt/NiFe.

Section S5: Angular dependent ST-FMR measurement for pristine Pt/NiFe

The angular dependent studies must be carefully analyzed before accurately assessing the torques in ST-FMR line-shape analysis as it requires careful attention from possible artefacts such as spin torque with different symmetries [2]. In V_{mix} signal, the contributions to expected angular dependence partially arise from AMR with sin (2ϕ) dependence, while the current-induced torque exhibit cos(ϕ) dependence. We performed angular dependent measurement of ST-FMR signal for Pt/NiFe sample from ϕ=0° to ϕ=360° by changing the direction of applied external DC magnetic field with respect to I_{rf} current of fixed frequency ~ 9 GHz at 15 dBm. The symmetric and antisymmetric components weight factors are extracted as a function of ϕ and plotted in Figure S4. Both symmetric and antisymmetric components yield the same angular dependence behavior, match well with in-plane excitation and fitted by sin(2ϕ)cos(ϕ) function.

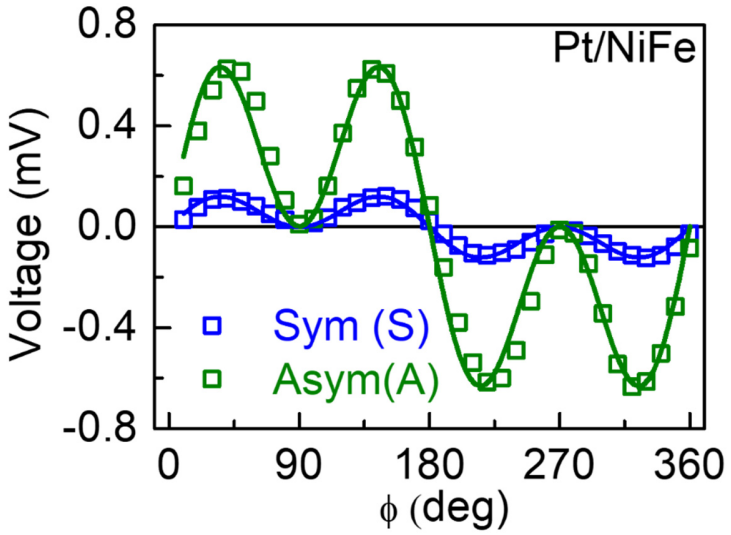

Figure S4: Angular dependence of symmetric and antisymmetric component of the ST-FMR voltage in Pt/NiFe.

Section S6: Spin pumping-inverse spin Hall voltage (SP-ISHV) measurement

We performed SP-ISHV measurements using coplanar waveguide based micro device as shown in Fig. S5(a). SP is defined as the injection of pure spin current into adjacent HM metallic layer (say Pt or Pt(S) in present case) due to magnetization precession in magnetic (NiFe) layer. The spin current injected into HM layer then gets converted into transverse charge current (dc voltage) by means of inverse-SHE. To minimize unwanted spin rectification signals, we employed out-of-plane excitation geometry as described in the schematic (Fig. S5b). Here careful alignment of H_{ext} at $\phi = 90^o$ or 270^o with respect to micro-strip leads to zero rectification-voltage contribution as it exhibits $\sin(2\phi)$ dependency while V_{ISHE} reaches to maximum amplitude, due to $\sin(\phi)$ dependence of SHE. As compared to measured V_{ISHE} signal across Pt/NiFe bilayer, Pt(S)/NiFe sample showed anticipated increase in V_{ISHE} amplitude for all rf frequencies (5-11 GHz, 15dBm), which are plotted respectively in Fig. S5c and S5d as a function of H_{ext}. The symmetric Lorentz line shape of V_{ISHE} spectrum along with sign reversal with equal magnitude under H_{ext} inversion implies its ISHE origin. In addition, the linear scaling of V_{ISHE} with microwave power with intercept at origin (0,0) is consistent with the theory, implying the measurements were performed in linear excitation regime [see inset of Fig. S5c]. One may notice that *f* dependent V_{ISHE} amplitude behaviour, common in both pristine and implanted Pt seems to differ from spin pumping theory that amplitude of voltage signal to be proportional to *f* [3]. However, the trend observed here is attributed to trajectory dependent J_s, as given by $J_s = \frac{2e}{\hbar} \times \frac{\hbar\omega}{4\pi} g^{\uparrow\downarrow} \sin^2\theta_C \left[2\omega \frac{\left(\gamma M_S + \sqrt{(\gamma M_S)^2 + (2\omega)^2}\right)}{(\gamma M_S)^2 + (2\omega)^2}\right]$ and we previously confirmed by independent determination of precession cone angle θ_C for wide $\omega = 2\pi f$ range that disclosed same trend in J_s values as well [4]. We then calculate spin mixing conductance $g^{\uparrow\downarrow}$, which is an important parameter that determines the spin pumping efficiency,

using $g^{\uparrow\downarrow} = \frac{4\pi M_s t\alpha}{g\mu_o\mu_B}$, where α accounts for increase in Gilbert damping due to loss in angular spin momentum during spin pumping. The $g^{\uparrow\downarrow}$ value approximately doubled from 26.2 nm^2 for Pt/NiFe to 49.8 nm^2 for Pt(S)/NiFe indicates increase in injected J_s for same resonance conditions. This increase of $g^{\uparrow\downarrow}$ value is ascribed to large spin relaxation and high spin-orbit-interaction in Pt(S)/NiFe system. Therefore, from V_{ISHE} values, estimated from Lorentzian fitting (shown in inset of Fig. S5d) and θ_{SH}^{LS}, we deduced 43% reduction in λ_{sd} in Pt(S), well-suited with the fundamental fact that spin diffusion length must decrease with higher resistivity in specimen [5].

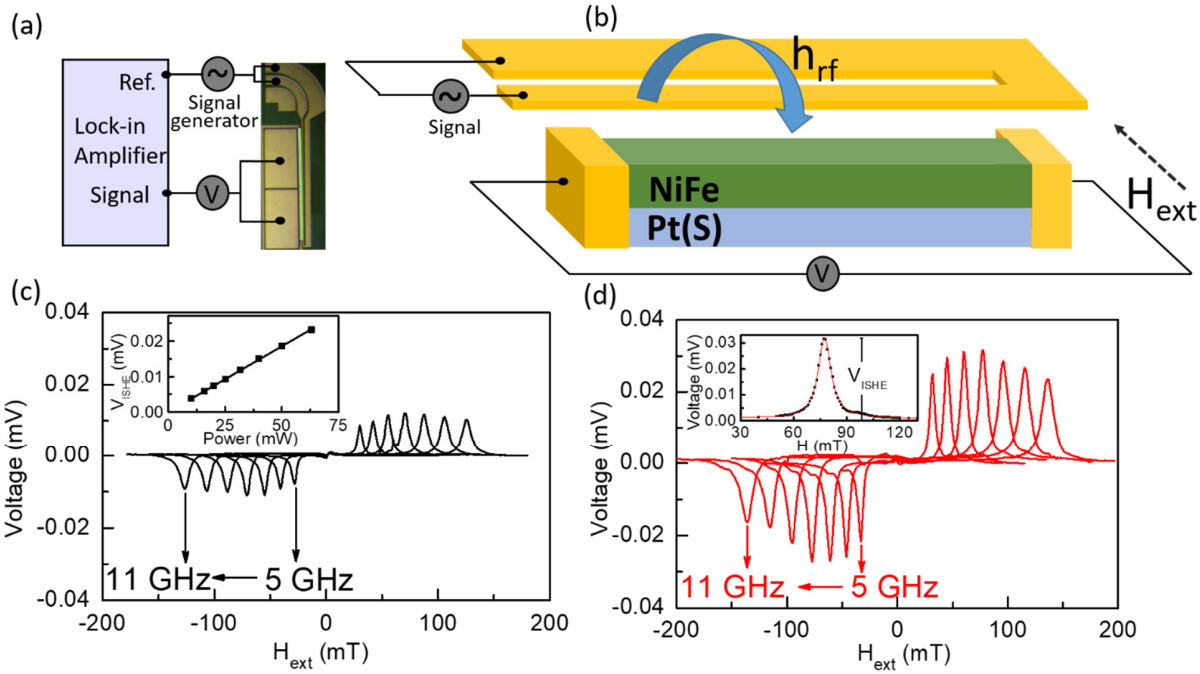

Figure S5: (a) Optical image of micro device with measurement setup. (b) Schematic illustration of out of plane excitation, opted to minimize unwanted spin rectification signals. Symmetric voltage spectra obtained for (c) Pt/NiFe and (d) Pt(S)/NiFe for frequency range (5-11 GHz) show approx. 3 times increase in signal amplitude. First inset shows V_{ISHE} as a linear function of rf power determined by Lorentzian fitting (second inset) of voltage signal at f = 8 GHz.

References

[1] T. Nan, S. Emori, C. T. Boone, X. Wang, T. M. Oxholm, J. G. Jones, B. M. Howe, G. J. Brown, N. X. Sun, *Phys. Rev. B* **2015**, *91*, 214416.

[2] M. H. Guimaraes, G. M. Stiehl, D. MacNeill, N. D. Reynolds, D. C. Ralph, *Nano Lett.* **2018**, *18*, 1311-1316.

[3] A. Azevedo, L. H. Vilela-Leão, R. L. Rodríguez-Suárez, A. L. Santos, S. M. Rezende, *Phys. Rev. B*, **2011**, *83***,** 144402.

[4] S. Gupta, R. Medwal, D. Kodama, K. Kondou, Y. Otani, Y. Fukuma, *Appl. Phys. Lett.* **2017**, *110***,** 022404.

[5] M. H. Nguyen, D. C. Ralph, R. A. Buhrman, *Phys. Rev. Lett.* **2016**, *116*, 126601.